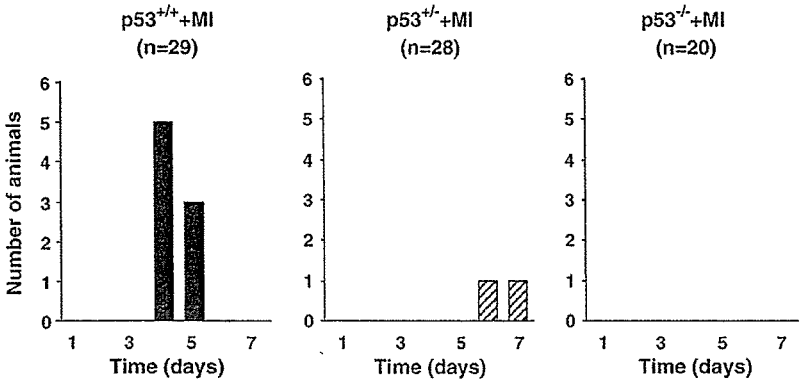

Fig. 3. The number of animals died of cardiac rupture in the $p53^{+/+}$+MI, $p53^{+/-}$+MI, and $p53^{-/-}$+MI mice.

antibody against phospho (Ser473)-Akt and Akt (Cell Signaling). In brief, the LV tissue was homogenized with the lysis buffer (25 mmol/L Tris, 150 mmol/L NaCl, 5 mmol/L EDTA, 1 mmol/L Na_3VO_4; pH 7.4). After centrifugation, equal amounts of protein (15 μg protein/lane), estimated by the Bradford method using a protein assay (Bio-Rad), were electrophoresed on a 12.5% SDS-polyacrylamide gel, and then electrophoretically transferred to a nitrocellulose membrane (Millipore). After blocking with 2.5% nonfat milk in TBS containing 0.1% Tween 20 at room temperature for 30 min, the membrane was incubated with the first antibody, and then with the peroxidase-linked second antibody (Santa Cruz). Chemiluminescence was detected with an ECL Western blot detection kit (Amersham Pharmacia) according to the manufacturer's recommendation.

2.5. Statistical analysis

All data are expressed as the means±S.E.M. A survival analysis was performed by the Kaplan–Meier method, and between-group difference in survival was tested by the logrank test. Between-group comparisons of the means were performed by one-way ANOVA, followed by *t*-tests. The Bonferroni's correction was done for multiple comparisons of the means.

3. Results

3.1. Experimental protocol 1: 7-day post-MI study

3.1.1. Survival and LV rupture

$p53^{+/-}$+MI and $p53^{-/-}$+MI mice had significantly better survival than $p53^{+/+}$+MI mice (Fig. 2). The number of the mice that died of LV rupture was significantly less in $p53^{-/-}$+MI and $p53^{+/-}$+MI than in $p53^{+/+}$+MI mice (Fig. 3). There were no deaths in the sham-operated groups. There were no significant differences in the survival rate among these 3 groups of survivor mice followed after 7 days up to 4 weeks.

3.2. Experimental protocol 2: 3-day post-MI study

3.2.1. Echocardiography and hemodynamics

The echocardiographic and hemodynamic data of the surviving mice at 3 days of MI are shown in Table 1. The LV diameters increased and fractional shortening decreased significantly in the $p53^{+/+}$+MI, $p53^{+/-}$+MI, and $p53^{-/-}$+

Table 1
Echocardiographic and hemodynamic data at 3 days after surgery

	$p53^{+/+}$+Sham	$p53^{+/-}$+Sham	$p53^{+/+}$+MI	$p53^{-/-}$+MI	$p53^{-/-}$+MI
Echocardiographic data					
n	7	7	13	12	7
Heart rate, bpm	491±3	487±5	492±7	493±5	484±15
LVEDD, mm	3.7±0.1	3.7±0.1	4.6±0.1**	4.7±0.1**	4.7±0.1**
LVESD, mm	2.3±0.0	2.3±0.1	3.9±0.1**	3.8±0.1**	3.8±0.1**
Fractional shortening, %	36.6±0.4	37.7±0.4	16.5±1.0**	17.9±0.7**	19.2±1.0**
Hemodynamic data					
n	7	7	11	10	5
Heart rate, bpm	492±14	491±10	481±15	490±13	494±6
Mean aortic pressure, mm Hg	79±4	79±2	77±2	79±2	74±1
LVEDP, mm Hg	1.3±0.4	1.3±0.4	12.0±1.9**	11.7±2.9**	10.2±2.8**
LV dP/dt_{max}, mm Hg/s	9055±1133	8299±332	5927±409**	5710±240**	6417±466**

MI, myocardial infarction. LV, left ventricular. EDD, end-diastolic diameter. ESD, end-systolic diameter. EDP, end-diastolic pressure. bpm, beats per min. Values are means±S.E.M. **$P<0.01$ vs. $p53^{+/-}$+Sham.

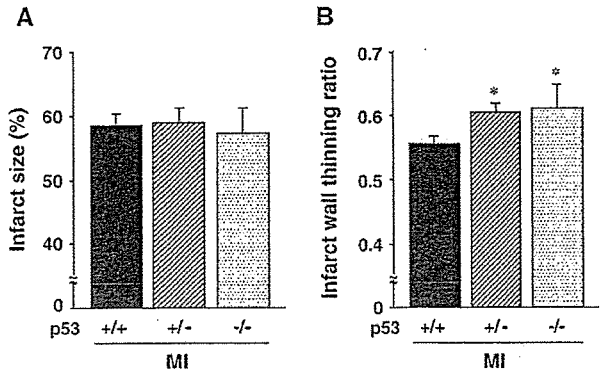

Fig. 4. Infarct size (A) and infarct wall thinning ratio (B) in $p53^{+/+}$-MI, $p53^{+/-}$MI, and $p53^{-/-}$MI mice ($n=6$ each). Values are means±S.E.M. *$P<0.05$ for difference from the $p53^{+/+}$+MI.

MI mice compared to sham operated mice. However, these changes were comparable among $p53^{+/+}$+MI, $p53^{+/-}$+MI, and $p53^{-/-}$+MI.

There was no significant difference in the heart rate and mean aortic blood pressure among 5 groups of mice. The LV end-diastolic pressure (EDP) increased and LV dP/dt_{max} decreased in $p53^{+/+}$+MI compared to sham, which was similarly observed in $p53^{+/-}$+MI and $p53^{-/-}$+MI.

3.2.2. Infarct size and wall thickness

The infarct size determined by the morphometric analysis at 3 days of MI was comparable among the $p53^{+/+}$+MI, $p53^{+/-}$+MI, and $p53^{-/-}$+MI ($n=6$ each) mice (Fig. 4A). Moreover, percentages of LV at risk (risk area/LV; 60.4±5.2% vs. 59.1±2.8%, P=NS) and the infarct size (infarct/risk area; 58.7±7.8% vs. 61.4±2.5%, P=NS) measured by Evans blue and TTC staining at 24 h of MI were also comparable between $p53^{+/-}$+MI and $p53^{+/+}$+MI ($n=5$ each).

The thickness of the infarcted LV wall and that of the noninfarcted LV in $p53^{-/-}$+MI were 0.43±0.02 and 0.70±0.03 mm, respectively, those in $p53^{+/-}$+MI were 0.41±0.02 and 0.67±0.03 mm, respectively, and those in $p53^{+/+}$+MI were 0.39±0.01 and 0.70±0.02 mm, respectively. Thus infarct wall thinning ratio, the thickness of the infarcted LV wall normalized to that of the noninfarcted LV, was significantly greater in $p53^{-/-}$+MI or $p53^{+/-}$+MI than in $p53^{+/+}$+MI (Fig. 4B).

3.2.3. Myocardial histopathology

MI mice had more infiltrating interstitial cells in the border zone and infarcted myocardium than sham-operated mice. However, the extent of infiltration was comparable among $p53^{+/+}$+MI, $p53^{+/-}$+MI, and $p53^{-/-}$+MI (Fig. 5A). Moreover, the infiltration of macrophages was similar between groups (Fig. 5B).

Interstitial fibrosis, measured as collagen volume fraction, in the infarcted as well as border zone LV was also comparable among $p53^{+/+}$+MI, $p53^{+/-}$+MI, and $p53^{-/-}$+MI (Fig. 6A).

3.2.4. MMPs

The zymographic MMP-2 and MMP-9 levels significantly increased in the infarcted LV from MI groups, however, no difference in this regard was seen between $p53^{+/+}$+MI and $p53^{+/-}$+MI mice (Fig. 6B).

3.2.5. Myocardial apoptosis

There were rare TUNEL-positive nuclei in sham-operated mice. The number of TUNEL-positive cells was increased in $p53^{+/+}$+MI, which was significantly prevented in $p53^{+/-}$+MI and $p53^{-/-}$+MI (Fig. 7A). In addition, DNA ladder appeared faint in the infarcted LV from $p53^{+/-}$+MI compared to that from $p53^{+/+}$+MI (Fig. 7B).

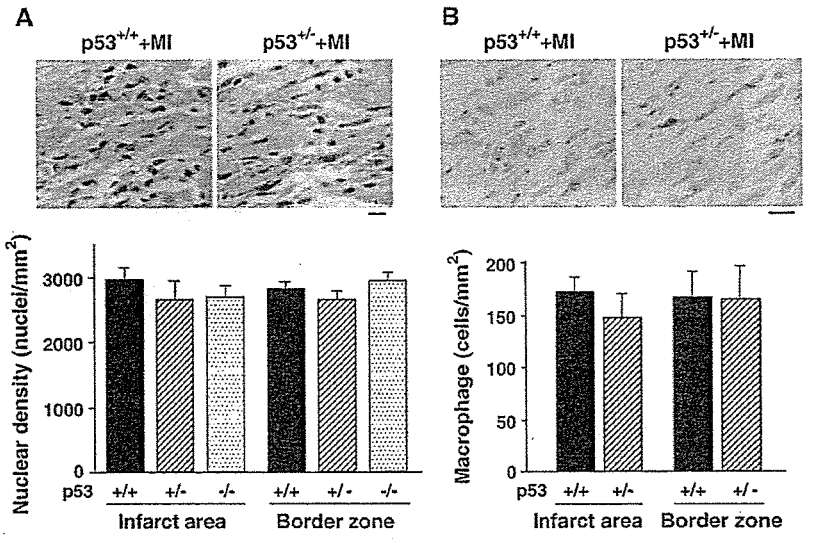

Fig. 5. Representative photomicrographs of LV sections and summary data for nuclear density of infiltrating cells stained with hematoxylin and eosin (A) and macrophages (B) at the infarct area and border zone. Scale bar, 10 μm. Values are means±S.E.M. ($n=6$ each).

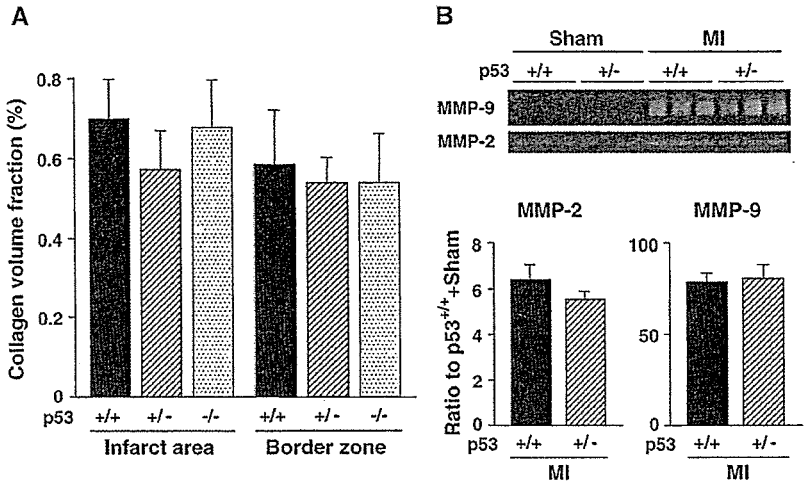

Fig. 6. (A) Summary data of collagen volume fraction at the infarcted area and border zone of LV tissue sections ($n=6$ for each). (B) Representative LV zymographic MMP-2 and MMP-9 levels and summary data at 3 days of MI ($n=6$ for each).

3.2.6. Akt protein

Either Akt protein (total) or phospho-Akt levels did not differ between 4 groups of $p53^{+/+}$+Sham, $p53^{+/-}$+Sham, $p53^{+/+}$+MI, and $p53^{+/-}$+MI mice (Fig. 8).

4. Discussion

The major new finding of the present study is the significant improvement in the survival of MI mice by the targeted deletion of p53 gene, which was mainly attributable to the inhibition of early LV rupture. After MI, p53-dependent apoptosis might contribute to the thinning of the infarct wall and eventual LV rupture. Our observations thus suggest that an anti-p53 strategy may be of therapeutic benefit against the evolution of cardiac rupture after MI.

Cardiac rupture is the most drastic and severe complication of acute MI. Following MI, a reparative process, infarct healing, is immediately initiated, including inflammatory cell infiltration, activation of MMPs, extracellular matrix remodeling and scar formation. Thinning of the infarcted wall and dilatation of LV cavity, which occur during the acute phase of MI, are termed as "infarct expansion" [1]. The delay or impairment of this process may jeopardize infarct healing, aggravate extracellular matrix remodeling, and cause cardiac rupture. Previous studies demonstrated that p53 was increased [8] and apoptosis of cardiac myocytes were detected in the infarcted regions during the

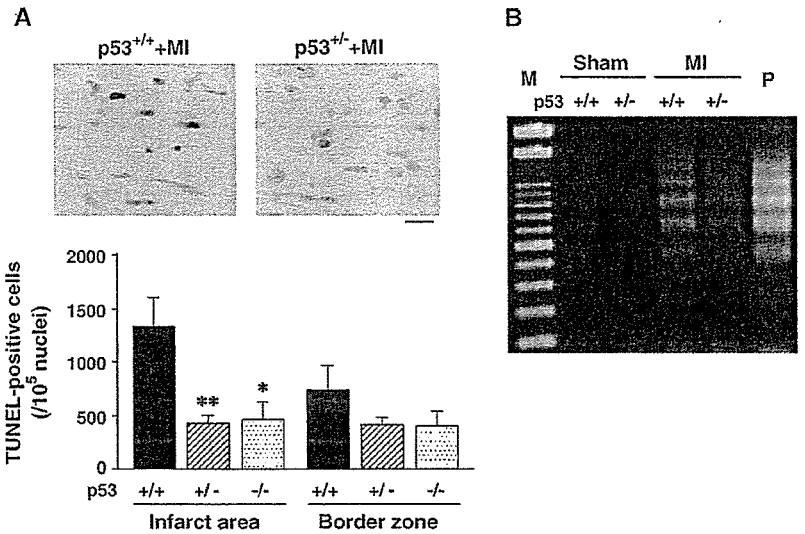

Fig. 7. (A) Representative photomicrographs of LV sections and summary data for the number of TUNEL-positive cells in the infarcted area and border zone of LV ($n=6$ each). Scale bar, 10 μm. Values are means±S.E.M. *$P<0.05$, **$P<0.01$ for difference from the $p53^{+/+}$+MI values. (B) DNA ladder indicative of apoptosis in the genomic DNA from the LV. M, marker. P, positive control.

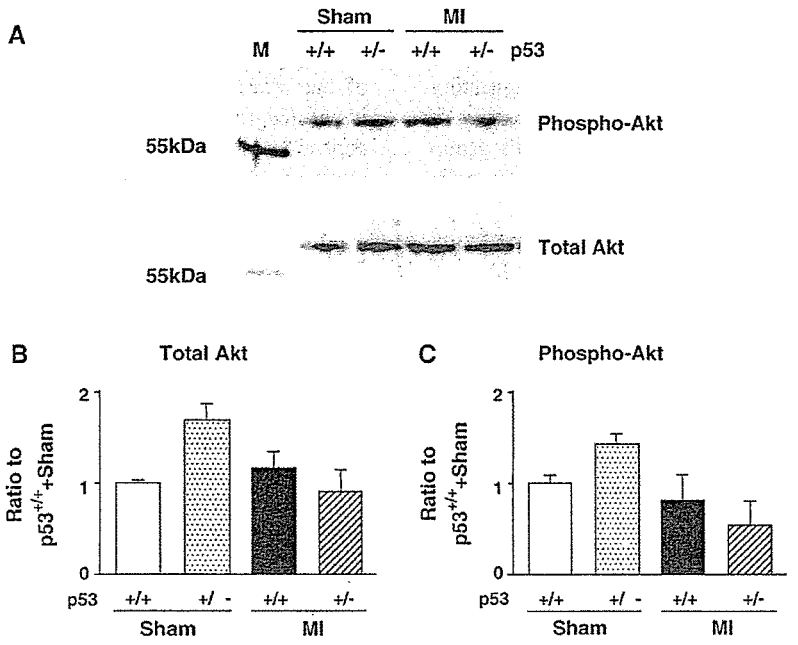

Fig. 8. (A) Representative Western blot analysis of Akt (total) and phospho-Akt protein levels in LV tissue obtained from 4 groups of $p53^{+/+}$+Sham, $p53^{+/-}$+Sham, $p53^{+/+}$+MI, and $p53^{+/-}$+MI mice. Summary data for total Akt (B) and phospho-Akt (C) protein levels in $p53^{+/+}$+Sham, $p53^{+/-}$+Sham, $p53^{+/+}$+MI, and $p53^{+/-}$+MI mice ($n=3$ for each). M, marker.

early days after MI [9,10]. Therefore, p53-dependent apoptosis at the infarcted myocardium may contribute to cardiac rupture. However, no previous studies have provided direct evidence supporting this notion. The present study has demonstrated that p53 is indeed involved in cardiac rupture after MI (Fig. 3) via mediating apoptosis (Fig. 7) and wall thinning at the infarct area (Fig. 4B).

The beneficial effects of p53 deletion were not due to its MI size-sparing effects because the infarct size was comparable between the $p53^{+/+}$ and $p53^{+/-}$ mice (Fig. 4A). Further, its effects might not be attributable to those on hemodynamics because the blood pressure and heart rate showed no alterations (Table 1). In addition, inflammatory cell infiltration and inadequate fibrosis have been postulated to cause myocyte separation in the infarct area, which may lead to eventual cardiac rupture [4]. However, the present study could not find any alterations in the infiltration of inflammatory cells or collagen deposition between $p53^{+/+}$ and $p53^{+/-}$ mice after MI (Figs. 5 and 6A). Further, even though recent studies have demonstrated that the inhibition of MMPs can prevent cardiac rupture [4,5], targeted deletion of p53 gene did not affect the increase in MMP-2 or MMP-9 activities in the post-MI hearts in the present study (Fig. 6B). These lines of evidence indicate that the inhibition of cardiac rupture in $p53^{+/-}$ mice was not due to the altered reparative process of extracellular matrix or the infiltration of inflammatory cells and further confirm the significance of attenuated apoptosis and infarct wall thinning in the prevention of cardiac rupture.

Previous experimental [9] and human [10] studies have detected TUNEL-positive cells in the post-MI hearts. Even though they implicated apoptosis in the pathogenesis of late LV remodeling after MI [19], it may also contribute to the early phase structural alterations known to occur within the infarct area, which is characterized by a significant net loss of cardiac myocytes as well as myocyte slippage and elongation [24]. However, the significance of myocardial apoptosis in this phase of MI has been mostly speculative. Thus the present study clearly demonstrated for the first time that p53-dependent apoptosis is involved not only in late remodeling after MI [19] but also in early cardiac rupture.

The present study was in contrast to the previous study by Bialik et al., in which myocyte apoptosis was not altered after MI in the hearts of mice nullizygous for p53 [25]. It is difficult, however, to find identical experimental conditions between their study and the present study by that would be necessary for a direct comparison; the age of the animals (6–8 weeks in the study by Bialik vs. 10–14 weeks in this study) and the time at which apoptosis was assessed (10 and 48 h vs. 3 days). In addition, the infarct size was comparable between $p53^{-/-}$ and $p53^{+/-}$ in the present study although it was not clearly mentioned in the study by Bialik. Although the present study demonstrated the survival benefit in p53 deletion, no survival data were provided in their study.

p53 is known to be dynamically regulated via Akt, a serine/threonine kinase, that promotes cell survival [26]. Specifically, proapoptotic stimulation leads to p53-dependent destruction of Akt whereas Akt activation leads to inhibition of p53. The state of this signaling network determines the fate of the cell to survive or to enter apoptosis or hypertrophy. However, either Akt protein

(total) or phospho-Akt levels did not differ between 4 groups of $p53^{+/+}$+Sham, $p53^{+/-}$+Sham, $p53^{+/+}$+MI, and $p53^{+/-}$+MI mice in the present study (Fig. 8), suggesting that Akt might not play a major role in myocyte apoptosis in this model. Moreover, a recent study by Dr. Field's group has demonstrated that p193 and p53 exert a cell cycle regulatory role in the adult heart [27]. In their studies, target expression of the p193 and/or the p53 dominant-interfering mutants increased cardiac myocyte DNA synthesis after MI in mice, suggesting that cardiac cell cycle reentry is regulated by these proapoptotic proteins. Therefore, we could not exclude the possibility that p193 might also be involved in post-MI remodeling.

Even though the previous studies reported a difference in the phenotype between $p53^{-/-}$ and $p53^{+/-}$ mice [15,16], the echocardiographic data (Table 1), hemodynamic data (Table 1), infarct size (Fig. 4), infarct wall thinning ratio (Fig. 4), nuclear density (Fig. 5), collagen volume fraction by myocardial histopathology (Fig. 6), and the number of TUNEL-positive cells (Fig. 7) were comparable between these 2 groups of mice in the present study. Based on these results, there might be a threshold in the effects of p53 gene expression on cardiac pathophysiology after MI.

There are several limitations to be acknowledged in this study. First, although p53 is activated in the post-MI hearts [8], the mechanisms responsible for this activation are not determined in the present study. One important aspect of ischemia is prolonged hypoxia, which has been shown to increase p53 expression and result in apoptosis in cultured cardiac myocytes [6]. Furthermore, oxidative stress, which is also increased in post-MI hearts, is a powerful inducer of apoptosis [28]. However, further studies are needed to clarify the mechanisms for the modulation of p53 after MI. Second, even though the previous study demonstrated that p53 expression was increased in post-MI rat hearts [8], the present study did not determine whether endogenous p53 expression was altered in post-MI mouse hearts. Third, p53-dependent apoptotic pathways may not be a sole mechanism for cardiac rupture after MI. Cardiac repair after MI is a highly complex process, involving diverse inflammatory and growth factor signaling pathways, and extracellular matrix remodeling. Thus the mechanisms other than p53 may be also involved in this deleterious complication. Fourth, echocardiographic assessment of LV function in mice is known to be difficult. However, intra- and interobserver variabilities of our echocardiographic measurements for LV cavity dimensions and fractional shortening were small and measurements were highly reproducible [14]. Therefore, our technique was capable of noninvasively assessing the LV structure and function in mice with a large MI.

Cardiac rupture usually occurs unexpectedly and is often fatal, thereby resulting in one of the major causes of in-hospital death in patients with acute MI. It is difficult to predict its occurrence by the previously reported clinical risk factors such as aging, hypertension, and delayed thrombolysis [29]. We found that target deletion of p53 had a significantly reduced cardiac rupture rate after MI. This was accompanied by a reduction of apoptosis and wall thinning of the infarcted myocardium. Our results may provide a novel insight regarding the pathophysiological role of p53-dependent apoptosis in cardiac rupture and thus help to establish an effective therapeutic strategy.

Acknowledgments

This study was supported in part by grants from the Ministry of Education, Science and Culture (Nos. 120670676, 14370230, 17390223). A part of this study was conducted in Kyushu University Station for Collaborative Research I and II.

References

[1] Pfeffer JM, Pfeffer MA, Fletcher PJ, Braunwald E. Progressive ventricular remodeling in rat with myocardial infarction. Am J Physiol 1991;260:H1406–14.
[2] Anzai T, Yoshikawa T, Shiraki H, Asakura Y, Akaishi M, Mitamura H, et al. C-reactive protein as a predictor of infarct expansion and cardiac rupture after a first Q-wave acute myocardial infarction. Circulation 1997;96:778–84.
[3] Przyklenk K, Connelly CM, McLaughlin RJ, Kloner RA, Apstein CS. Effect of myocyte necrosis on strength, strain, and stiffness of isolated myocardial strips. Am Heart J 1987;114:1349–59.
[4] Heymans S, Luttun A, Nuyens D, Theilmeier G, Creemers E, Moons L, et al. Inhibition of plasminogen activators or matrix metalloproteinases prevents cardiac rupture but impairs therapeutic angiogenesis and causes cardiac failure. Nat Med 1999;5:1135–42.
[5] Matsumura S, Iwanaga S, Mochizuki S, Okamoto H, Ogawa S, Okada Y. Targeted deletion or pharmacological inhibition of MMP-2 prevents cardiac rupture after myocardial infarction in mice. J Clin Invest 2005;115:599–609.
[6] Long X, Boluyt MO, Hipolito ML, Lundberg MS, Zheng JS, O'Neill L, et al. p53 and the hypoxia-induced apoptosis of cultured neonatal rat cardiac myocytes. J Clin Invest 1997;99:2635–43.
[7] Polyak K, Xia Y, Zweier JL, Kinzler KW, Vogelstein B. A model for p53-induced apoptosis. Nature 1997;389:300–5.
[8] Oskarsson HJ, Coppey L, Weiss RM, Li WG. Antioxidants attenuate myocyte apoptosis in the remote non-infarcted myocardium following large myocardial infarction. Cardiovasc Res 2000;45:679–87.
[9] Kajstura J, Cheng W, Reiss K, Clark WA, Sonnenblick EH, Krajewski S, et al. Apoptotic and necrotic myocyte cell deaths are independent contributing variables of infarct size in rats. Lab Invest 1996;74:86–107.
[10] Saraste A, Pulkki K, Kallajoki M, Henriksen K, Parvinen M, Voipio-Pulkki LM. Apoptosis in human acute myocardial infarction. Circulation 1997;95:320–3.
[11] Mayr U, Mayr M, Li C, Wernig F, Dietrich H, Hu Y, et al. Loss of p53 accelerates neointimal lesions of vein bypass grafts in mice. Circ Res 2002;90:197–204.
[12] Donehower LA, Harvey M, Slagle BL, McArthur MJ, Montgomery CA, Butel JS, et al. Mice deficient for p53 are developmentally normal but susceptible to spontaneous tumours. Nature 1992;356:215–21.
[13] Ducharme A, Frantz S, Aikawa M, Rabkin E, Lindsey M, Rohde LE, et al. Targeted deletion of matrix metalloproteinase-9 attenuates left ventricular enlargement and collagen accumulation after experimental myocardial infarction. J Clin Invest 2000;106:55–62.
[14] Shiomi T, Tsutsui H, Hayashidani S, Suematsu N, Ikeuchi M, Wen J, et al. Pioglitazone, a peroxisome proliferator-activated receptor-

gamma agonist, attenuates left ventricular remodeling and failure after experimental myocardial infarction. Circulation 2002;106:3126–32.
[15] Armstrong JF, Kaufman MH, Harrison DJ, Clarke AR. High-frequency developmental abnormalities in p53-deficient mice. Curr Biol 1995;5:931–6.
[16] Rotter V, Schwartz D, Almon E, Goldfinger N, Kapon A, Meshorer A, et al. Mice with reduced levels of p53 protein exhibit the testicular giant-cell degenerative syndrome. Proc Natl Acad Sci U S A 1993;90:9075–9.
[17] Pfeffer MA, Pfeffer JM, Fishbein MC, Fletcher PJ, Spadaro J, Kloner RA, et al. Myocardial infarct size and ventricular function in rats. Circ Res 1979;44:503–12.
[18] Patten RD, Aronovitz MJ, Deras-Mejia L, Pandian NG, Hanak GG, Smith JJ, et al. Ventricular remodeling in a mouse model of myocardial infarction. Am J Physiol 1998;274:H1812–20.
[19] Sam F, Sawyer DB, Chang DL, Eberli FR, Ngoy S, Jain M, et al. Progressive left ventricular remodeling and apoptosis late after myocardial infarction in mouse heart. Am J Physiol Heart Circ Physiol 2000;279:H422–8.
[20] Ikeuchi M, Tsutsui H, Shiomi T, Matsusaka H, Matsushima S, Wen J, et al. Inhibition of TGF-beta signaling exacerbates early cardiac dysfunction but prevents late remodeling after infarction. Cardiovasc Res 2004;64:526–35.
[21] Delyani JA, Robinson EL, Rudolph AE. Effect of a selective aldosterone receptor antagonist in myocardial infarction. Am J Physiol Heart Circ Physiol 2001;281:H647–54.
[22] Lindsey ML, Gannon J, Aikawa M, Schoen FJ, Rabkin E, Lopresti-Morrow L, et al. Selective matrix metalloproteinase inhibition reduces left ventricular remodeling but does not inhibit angiogenesis after myocardial infarction. Circulation 2002;105:753–8.
[23] Hayashidani S, Tsutsui H, Ikeuchi M, Shiomi T, Matsusaka H, Kubota T, et al. Targeted deletion of MMP-2 attenuates early LV rupture and late remodeling after experimental myocardial infarction. Am J Physiol Heart Circ Physiol 2003;285:H1229–35.
[24] Li Q, Li B, Wang X, Leri A, Jana KP, Liu Y, et al. Overexpression of insulin-like growth factor-1 in mice protects from myocyte death after infarction, attenuating ventricular dilation, wall stress, and cardiac hypertrophy. J Clin Invest 1997;100:1991–9.
[25] Bialik S, Geenen DL, Sasson IE, Cheng R, Horner JW, Evans SM, et al. Myocyte apoptosis during acute myocardial infarction in the mouse localizes to hypoxic regions but occurs independently of p53. J Clin Invest 1997;100:1363–72.
[26] Sussman MA, Anversa P. Myocardial aging and senescence: where have the stem cells gone? Annu Rev Physiol 2004;66:29–48.
[27] Nakajima H, Nakajima HO, Tsai SC, Field LJ. Expression of mutant p193 and p53 permits cardiomyocyte cell cycle reentry after myocardial infarction in transgenic mice. Circ Res 2004;94:1606–14.
[28] von Harsdorf R, Li PF, Dietz R. Signaling pathways in reactive oxygen species-induced cardiomyocyte apoptosis. Circulation 1999; 99:2934–41.
[29] Maggioni AP, Maseri A, Fresco C, Franzosi MG, Mauri F, Santoro E, et al. Age-related increase in mortality among patients with first myocardial infarctions treated with thrombolysis. The Investigators of the Gruppo Italiano per lo Studio della Sopravvivenza nell'Infarto Miocardico (GISSI-2). N Engl J Med 1993;329:1442–8.

Targeted Deletion of Matrix Metalloproteinase 2 Ameliorates Myocardial Remodeling in Mice With Chronic Pressure Overload

Hidenori Matsusaka, Tomomi Ide, Shouji Matsushima, Masaki Ikeuchi, Toru Kubota, Kenji Sunagawa, Shintaro Kinugawa, Hiroyuki Tsutsui

Abstract—Matrix metalloproteinases (MMPs) play an important role in the extracellular matrix remodeling. Experimental and clinical studies have demonstrated that MMP 2 and 9 are upregulated in the dilated failing hearts and involved in the development and progression of myocardial remodeling. However, little is known about the role of MMPs in mediating adverse myocardial remodeling in response to chronic pressure overload (PO). We, thus, hypothesized that selective disruption of the MMP 2 gene could ameliorate PO-induced cardiac hypertrophy and dysfunction in mice. PO hypertrophy was induced by transverse aortic constriction (TAC) in male MMP 2 knockout (KO) mice (n=10) and sibling wild-type (WT) mice (n=9). At 6 weeks, myocardial MMP 2 zymographic activity was 2.4-fold increased in WT+TAC, and this increase was not observed in KO+TAC, with no significant alterations in other MMPs (MMP 1, 3, 8, and 9) or tissue inhibitors of MMPs (1, 2, 3, and 4). TAC resulted in a significant increase in left ventricular (LV) weight and LV end-diastolic pressure (EDP) with preserved systolic function. KO+TAC mice exerted significantly lower LV weight/body weight (4.2±0.2 versus 5.0±0.2 mg/g; $P<0.01$), lung weight/body weight (4.9±0.2 versus 6.2±0.4 mg/g; $P<0.01$), and LV end-diastolic pressure (4±1 versus 10±2 mm Hg; $P<0.05$) than WT+TAC mice despite comparable aortic pressure. KO+TAC mice had less myocyte hypertrophy (cross-sectional area; 322±14 versus 392±14 μm^2; $P<0.01$) and interstitial fibrosis (collagen volume fraction; 3.3±0.5 versus 8.2±1.0%; $P<0.01$) than WT+TAC mice. MMP 2 plays an important role in PO-induced LV hypertrophy and dysfunction. The inhibition of MMP 2 activation may, therefore, be a useful therapeutic strategy to manage hypertensive heart disease. (***Hypertension.* 2006;47:711-717.**)

Key Words: hypertrophy ■ heart failure ■ fibrosis ■ extracellular matrix ■ hypertension, experimental ■ myocardium

Left ventricular (LV) hypertrophy is an adaptive process that compensates for pressure overload (PO) caused by hypertension or valvular heart disease, such as aortic stenosis. This remodeling process consists of hypertrophic changes of cardiac myocytes and abnormalities of the extracellular matrix (ECM) network, which are both responsible for changes in systolic and diastolic function.[1]

The dynamic synthesis and breakdown of ECM proteins play an important role in adverse myocardial remodeling. In particular, the increased expression and activation of the matrix metalloproteinases (MMPs) have been shown in various forms of heart failure and implicated in the process of myocardial remodeling that is characteristic of developing heart failure.[2] Despite a number of studies implicating MMPs in cardiac pathophysiology, little is known about the role of MMP in the development of myocardial remodeling in response to chronic PO. MMP 2 and 9 expression has been shown to be enhanced in pressure-overloaded cardiac hypertrophy in spontaneously hypertensive rats[3] and in Dahl salt-sensitive hypertensive rats.[4] Similar upregulation of MMPs has been also observed in human pressure-overloaded hearts because of aortic stenosis.[5] Recently, Heymans et al[6] have demonstrated that MMP 9 is involved in cardiac remodeling associated with hypertension. However, MMP-9 is mainly expressed in such infiltrating inflammatory cells as neutrophils and macrophages.[7] Conversely, MMP 2 is ubiquitously distributed in cardiac myocytes and fibroblasts.[8] Therefore, MMP 2 may also play an important role in the development and progression of myocardial remodeling in response to PO. However, no previous studies have yet determined the pathophysiological significance of MMP 2 in this disease state.

In the present study, we evaluated the effects of a targeted deletion of the MMP 2 gene on both LV structural and

Received November 28, 2005; first decision December 13, 2005; revision accepted January 3, 2006.

From the Department of Cardiovascular Medicine (H.M., T.I., S.M., M.I., T.K., K.S.), Graduate School of Medical Sciences, Kyushu University, Fukuoka; and Department of Cardiovascular Medicine (S.K., H.T.), Hokkaido University Graduate School of Medicine, Sapporo, Japan.

Correspondence to Hiroyuki Tsutsui, Dept of Cardiovascular Medicine, Hokkaido University Graduate School of Medicine, Kita-15, Nishi-7, Kita-ku, Sapporo 060-8638, Japan. E-mail htsutsui@med.hokudai.ac.jp

Hypertension **is available at http://www.hypertensionaha.org** **DOI: 10.1161/01.HYP.0000208840.30778.00**

functional alterations during pressure-overloaded cardiac hypertrophy. To ensure selective and long-term complete inhibition of MMP 2, we used MMP 2 knockout (KO) mice.[9–11] The most effective way to evaluate the contribution of the specific MMP and obtain the direct evidence for a role of MMP is through gene manipulation instead of MMP inhibitor.

Methods

Experimental Animals

The study was approved by our Institutional Animal Research Committee and conformed to the animal care guidelines of the American Physiological Society. We used the progeny of homozygous breeding pairs of C57BL/6J mice with targeted disruption of MMP 2 ranging in age from 11 to 14 weeks old.[10] The mutation heterozygous mice were obtained by crossing the chimeras to C57BL/6J mice. Heterozygotes were backcrossed to C57BL/6J 1 to 5 times and then crossed to obtain the mutation homozygous mice. The original breeding pairs used to develop the mice for this study were obtained from Dr Shigeyoshi Itohara (Laboratory for Behavioral Genetics, RIKEN, Tsukuba, Japan).

Transverse Aortic Constriction

Transverse aortic constriction (TAC) was performed in male MMP 2 KO and sibling wild-type (WT) mice as described previously.[12] Briefly, after anesthetizing by tribromoethanol/amylene hydrate (Avertin; 2.5% weight/volume, 8 μL/g IP), mice were intubated and ventilated, and a thoracotomy was performed via the second intercostal space at the left upper sternal border. The transverse aortic arch was ligated between the innominate and left common carotid arteries with an overlying 28-gauge needle, which, after removal of the needle, left a reproducible discrete region of stenosis. Sham-operated mice underwent a similar procedure without ligation of the aorta.

Tail clips and a PCR protocol to confirm the genotype were performed by a group of investigators. Next, TAC was induced in these mice by another subset of investigators, who were not informed of the genotyping results. This assignment procedure was performed using numeric codes to identify the animals.

MMPs and Tissue Inhibitors of MMPs

First, the myocardial MMP levels, including MMP 2 and MMP 9, were determined in the left ventricle (LV) using gelatin zymography as described previously.[13] The LV myocardial samples were homogenized (≈30-s bursts) in 1 mL of an ice-cold extraction buffer containing cacodylic acid (10 mmol/L), NaCl (0.15 mol/L), $ZnCl_2$ (20 mmol/L), NaN_2 (1.5 mmol/L), and 0.01% Triton X-100 (pH 5.0). The homogenate was then centrifuged (4°C, 10 minutes, 10 000*g*) and the supernatant decanted and saved on ice. The pH levels of the samples were adjusted to 7.5 using Tris (1 mol/L). The final protein concentration of the myocardial extracts was determined using a standardized colorimetric assay. The extracted samples were then aliquoted and stored at −80°C until the time of assay. The myocardial extracts were then directly loaded onto electrophoretic gels (SDS-PAGE) containing 1 mg/mL of gelatin under nonreducing conditions. The myocardial extracts at a final protein content of 5 μg were loaded onto the gels using a 3:1 sample buffer (10% SDS, 4% sucrose, 0.25 mol/L Tris-Cl, and 0.1% bromophenol blue ≤pH 6.8]). The gels were run at 15 mA/gel through the stacking phase (4%) and at 20 mA/gel for the separating phase (10%), whereas the running buffer temperature was maintained at 4°C. After SDS-PAGE, the gels were washed twice in 2.5% Triton X-100 for 30 minutes each, rinsed in water, and incubated for 24 hours in a substrate buffer at 37°C (50 mmol/L Tris-HCl, 5 mmol/L, $CaCl_2$, and 0.02% NaN_3 [pH 7.5]). After incubation, the gels were stained with Coomassie brilliant blue R-250. The zymograms were digitized, and the size-fractionated bands, which indicated the MMP proteolytic levels, were measured by the integrated optical density in a rectangular region of interest.

Next, the mRNA levels of myocardial MMPs including MMP 1, 2, 3, 8, and 9 as well as tissue inhibitors of MMPs (TIMPs) including TIMP 1, 2, 3, and 4 were determined by multiprobe ribonuclease protection assay (RiboQuant, PharMingen). Each value was normalized to that of glyceraldehydes-3-phosphate-dehydrogenase in each template set as an internal control, followed by calculation as a ratio to WT+Sham. The amount of tissue was limited in mice and, thus, tissue needed to be divided so that all of the biochemical analyses could be performed.

Echocardiographic and Hemodynamic Measurements

Echocardiographic studies were performed under light anesthesia with tribromoethanol/amylene hydrate (Avertin; 2.5% weight/volume, 8 μL/g IP) and spontaneous respiration as described previously.[14] A 2D parasternal short-axis view of the LV was obtained at the level of the papillary muscles. In general, the best views were obtained with the transducer lightly applied to the mid-upper left anterior chest wall. The transducer was then gently moved cephalad or caudad and angulated until desirable images were obtained. After confirming that the imaging was on axis (based on roundness of the LV cavity), 2D targeted M-mode tracings were recorded at a paper speed of 50 mm/s. Two consecutive heartbeats of each frame were analyzed to measure the wall thickness and end-diastolic (EDD) and end-systolic (ESD) internal dimensions of the LV. LV fractional shortening (FS) was calculated as LV EDD minus LV ESD normalized for LV EDD and was taken as an index of LV systolic performance. Echocardiographic LV mass was calculated according to the standard cube formula as described previously.[15] Our previous validation study has shown that the intraobserver and interobserver variabilities of our echocardiographic measurements for LV cavity dimensions and FS were small, and measurements made in the same animals on separate days were highly reproducible.[14] Next, a 1.4-Fr micromanometer-tipped catheter (Millar) was inserted into the right carotid artery and then was advanced into the LV to measure the LV pressures. Arterial blood pressure and heart rate were also measured with the use of a noninvasive tail-cuff system (BP-98A, Softron).[16]

Organ Weight and Histopathology

After in vivo echocardiographic and hemodynamic studies, the heart and lung were excised, and their weights were determined. The heart was dissected into the right and left ventricles, including the septum. From the mid-LV transverse sections, 5-μm sections were cut and stained with hematoxylin/eosin and Masson's trichrome to determine the myocyte cross-sectional area and collagen volume fraction. To measure the myocyte cross-sectional area, each section was photographed using a microscope and magnified (final magnification: ×750). Connective tissue and muscle areas were identified, and the profile margin of 30 to 40 myocytes cut into cross-sections was manually traced and digitized. The digitized profiles were transferred to a personal computer that calculated the area. Three to 4 fields were randomly selected from 2 to 3 coronal sections of each heart. Thus, ≈100 to 200 myocytes were measured for each animal, and the mean myocyte cross-sectional area was calculated.[17] Collagen volume fraction was measured at ≈5 to 7 fields for each heart.[18] Within each field, segments representing connective tissue and myocyte were identified and manually traced by using a digitizing pad with a computer to calculate the traced area. Collagen volume fraction was then calculated for the heart as the sum of all of the connective tissue areas divided by the sum of all of the connective tissue and muscle areas in all fields. Collagen surrounding intramyocardial coronary arteries was excluded from the analysis.

Statistical Analysis

All of the data are expressed as the mean±SEM. Between-group comparisons of the means were performed by 1-way ANOVA, followed by *t* tests. The Bonferroni's correction was done for multiple comparisons of the means.

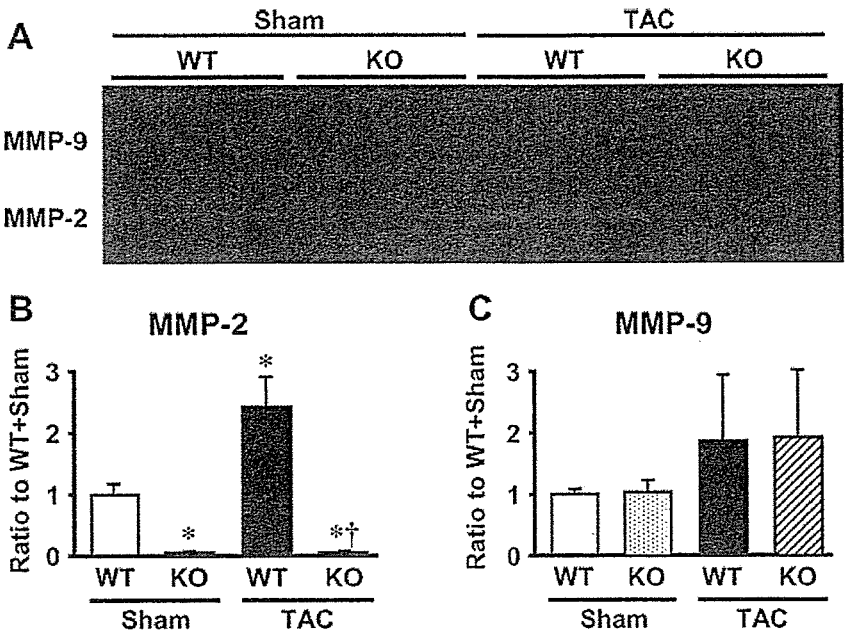

Figure 1. (A) Representative gelatin zymography of the LV from 4 groups of WT+Sham, KO+Sham, WT+TAC, and KO+TAC mice. (B and C) Densitometric analysis of MMP-2 (B) and MMP-9 (C) zymographic activity (n=3 each). Data are expressed as the ratio to WT+Sham values run concurrently on the same gel. Values are mean±SEM. *P<0.05 vs WT+Sham; †P<0.01 vs WT+TAC.

Results

MMPs and TIMPs

At 6 weeks of TAC, the zymographic MMP 2 levels increased by 2.4-fold compared with WT+Sham mice (Figure 1). As expected, MMP 2 activity was not detected in KO+Sham and KO+TAC mice. Importantly, the MMP 9 zymographic levels did not differ between WT+TAC and KO+TAC.

Again, the MMP 2 mRNA levels significantly increased in the WT+TAC compared with WT+Sham (Figure 2). This increase was not observed in KO+TAC. These results were consistent with those observed in gelatin zymography (Figure 1). Other MMPs, including MMP 1, 3, 8, and 9, were not altered in these mice (Figure 2). The changes of TIMPs (TIMP 1, 2, 3, and 4) were also comparable between WT+TAC and KO+TAC.

Echocardiography

The presence or absence of MMP 2 gene did not affect baseline heart rate or echocardiographic parameters in Sham mice (Table 1). TAC significantly increased LV wall thickness (Table 1) and echocardiographic LV mass (Figure 3) without affecting LV diameters or FS in WT+TAC. These LV hypertrophic changes in WT+TAC were significantly ameliorated in KO+TAC.

Hemodynamics

LV systolic pressure was markedly elevated by TAC (Table 2). However, there was no significant difference in LV systolic pressure between WT+TAC and KO+TAC mice. LV EDP increased significantly in WT+TAC mice, and this increase was significantly attenuated in KO+TAC mice.

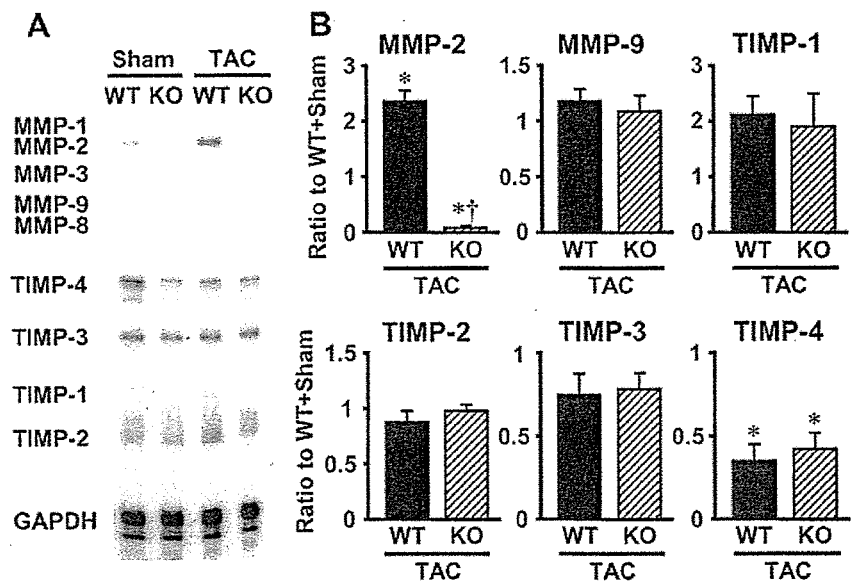

Figure 2. (A) Representative image of myocardial gene expression of MMPs and TIMPs. (B) Densitometric analysis of MMP and TIMP gene expression from WT+TAC (n=5) and KO+TAC (n=4). Each value was normalized to that of glyceraldehydes-3-phosphate-dehydrogenase in each template set as an internal control and expressed as the ratio to WT+Sham (n=3). Values are mean±SEM. *P<0.01 vs WT+Sham; †P<0.01 vs WT+TAC.

TABLE 1. Echocardiographic Data

Variable	WT+Sham (n=6)	KO+Sham (n=6)	WT+TAC (n=9)	KO+TAC (n=10)
Heart rate, bpm	469±10	467±13	475±8	470±6
LV EDD, mm	3.6±0.1	3.6±0.1	3.7±0.1	3.6±0.1
LV ESD, mm	2.2±0.1	2.2±0.1	2.4±0.1	2.3±0.1
Fractional shortening, %	37.2±0.8	36.3±1.0	35.1±0.9	35.5±0.7
Anterior wall thickness, mm	0.70±0.03	0.70±0.03	0.99±0.02*†	0.84±0.03*†‡
Posterior wall thickness, mm	0.77±0.02	0.78±0.02	1.04±0.02*†	0.92±0.03*†‡

Sham indicates sham operation without ligation of the aorta. Values are mean±SEM.
*P<0.01 vs WT+Sham; †P<0.01 vs KO+Sham; ‡P<0.01 vs WT+TAC.

Organ Weights

In agreement with echocardiographic LV mass (Figure 3), TAC increased LV weight in WT mice (Figure 4A). Furthermore, in accordance with LV EDP, lung weight/body weight, indicative of pulmonary congestion, increased significantly in WT+TAC (Figure 4B). In KO+TAC, both increased LV and lung weights were significantly reduced.

Histopathology

Masson's trichrome staining showed the increase in myocyte size and interstitial collagen volume fraction in WT+TAC mice compared with WT+Sham mice (Figure 5). The selective disruption of the MMP 2 gene significantly ameliorated myocyte hypertrophy and interstitial fibrosis by TAC. Similarly, picrosirius staining also demonstrated collagen deposition in the interstitial areas in LV sections from WT+TAC mice and the amelioration of interstitial fibrosis in KO+TAC mice (data not shown).

Discussion

In the present study, we demonstrated that the selective disruption of the MMP 2 gene ameliorated LV remodeling, such as myocyte hypertrophy and interstitial fibrosis in TAC mice, thus providing direct evidence that MMP 2 is involved in mediating PO-induced cardiac hypertrophy. These beneficial effects of MMP 2 inhibition occurred without affecting hemodynamics.

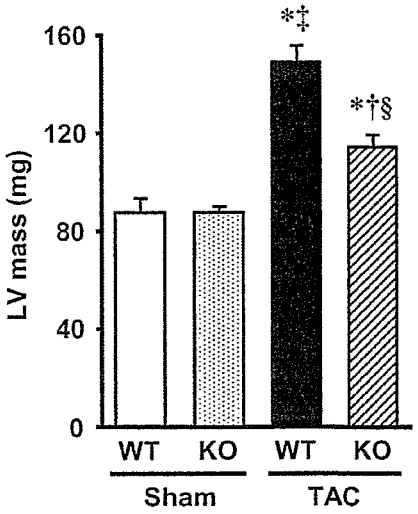

Figure 3. Echocardiographic LV mass from 4 groups of WT+Sham (n=6), KO+Sham (n=6), WT+TAC (n=9), and KO+TAC (n=10) mice. Values are mean±SEM. *P<0.01 vs WT+Sham; †P<0.05, ‡P<0.01 vs KO+Sham; §P<0.01 vs WT+TAC.

Upregulation of MMP 2 in PO Hypertrophy

The present study demonstrated that the MMP 2 gene expression and gelatinolytic activities were upregulated in the myocardium during PO (Figures 1 and 2). These findings, coupled with past reports, suggest that an increase in myocardial MMP levels is a fairly uniform event in myocardial remodeling.[2,3,6,19,20] Although the mechanisms responsible for this activation remain to be determined, cellular constituents of cardiac muscle, including fibroblasts, inflammatory cells, and myocytes, are known to be capable of expressing MMP 2 in response to specific stimuli, including mechanical stress.[9,21]

Role of MMP 2 in PO Hypertrophy

Alterations in the expression and activity of MMP 2 have been demonstrated in a number of pathophysiological conditions, such as myocardial infarction (MI) and heart failure. Our previous study[10] and a recent study by Matsumura et al[22] have demonstrated that the inhibition of MMP 2 activity improves the survival rate after acute MI by preventing cardiac rupture and delays after MI remodeling. A recent study by Wang et al[23] has shown that cardiac-specific, constitutively active MMP 2 expression leads to impaired contraction and diminished responses to inotropic stimulation, indicating that MMP 2 can directly impair cardiac function in the absence of superimposed injury.

Broad-spectrum pharmacological inhibition of MMPs significantly attenuated myocardial remodeling associated with chronic volume overload[3] or hypertension.[19] However, the most effective way to evaluate the contribution of the specific MMP and to obtain the direct evidence for a role of MMP in myocardial remodeling and failure is through such gene manipulation as that used in the present study. As expected, no MMP 2 expression was observed in the myocardium from KO mice in this study (Figures 1 and 2). Thus, the present study could investigate the effects of selective disruption of the MMP 2 gene on the development of myocardial hypertrophy induced by PO.

The most striking finding of the present study was the inhibition of myocardial hypertrophy in MMP 2 KO mice

TABLE 2. Hemodynamic Data

Variable	WT+Sham (n=6)	KO+Sham (n=6)	WT+TAC (n=9)	KO+TAC (n=10)
Heart rate, bpm	503±3	504±5	507±6	512±6
Arterial blood pressure, mm Hg	73±2	76±5	74±2	71±2
LV systolic pressure, mm Hg	104±4	104±3	202±6*†	196±9*†
LVEDP, mm Hg	1.5±1.2	2.4±0.9	9.8±2.2*†	3.5±0.7‡

Sham indicates sham operation without ligation of the aorta. Values are mean±SEM.
*P<0.01 vs WT+Sham; †P<0.01 vs KO+Sham; ‡P<0.05 vs WT+TAC.

under PO (Figures 3 through 5). Our previous studies demonstrated the beneficial effects of MMP 2 deletion also on postinfarct LV remodeling and failure.[10] Similar to the present study, both myocyte hypertrophy and interstitial collagen accumulation were ameliorated in the MMP 2–deficient mice after MI. Moreover, the present study is consistent with previous studies from other laboratories, which demonstrated the involvement of myocardial MMP in heart failure.[2,24,25] Therefore, the present study builds on these past reports by demonstrating that MMP inhibition attenuated myocardial remodeling that occurred also under PO.

The present study demonstrated that increased MMP 2 activity was associated with the interstitial fibrosis in pressure-overloaded LV and the selective inhibition of MMP 2, indeed, ameliorated these changes (Figure 5). Theoretically, an increase in MMP activity would result in a decrease in the MMP substrate, collagens, whereas an inhibition of MMP would result in an increase in collagens. However, in agreement with previous studies,[10] an increase in MMP 2 activity was accompanied by increased fibrosis in our model of LV hypertrophy, which is probably because of the direct proteolysis of myocardial matrix components, as well as by facilitating a profibrotic response. In fact, the selective disruption of the MMP 2 gene did attenuate interstitial fibrosis. Although the present study could not provide the definite explanation for these paradoxical findings, this might be because of the fact that the total ECM collagen content is a complex function of both synthesis and degradation.

In addition to interstitial fibrosis, myocyte cellular hypertrophy was also ameliorated by the selective blockade of the MMP 2 gene (Figure 5), suggesting that myocardial induction of MMP 2 is involved in the development of myocyte hypertrophy during PO. Recently, Heymans et al[6] demonstrated that MMP 9 gene inactivation reduced hypertrophic changes in cardiac myocytes during acute PO. These results suggest that there is an intimate link between MMPs and the myocyte hypertrophic process, which might be mediated, at least in part, by the tissue infiltration of inflammatory cells. However, the precise role of MMPs in the development of myocyte hypertrophy has not been fully explored. MMPs may be involved in a complex myocyte–matrix interaction, because the basement membrane components, collagen IV and laminin, are the substrates for MMP 2 and MMP 9.[26] Thus, increased MMP 2 activity within the myocardium can contribute to the discontinuity of the basement membrane, thereby disrupting the normal myocyte-matrix interface. The findings that MMP inhibition limited the degree of myocyte hypertrophy raise an issue requiring additional studies.

Limitations

There are several issues to be acknowledged as a limitation in this study. First, although in vivo assessment of LV function with echocardiography is feasible and reproducible in the mouse, it might still be difficult to interpret the indices of LV function. However, our validation study has shown that the intraobserver and interobserver variabilities of our echocar-

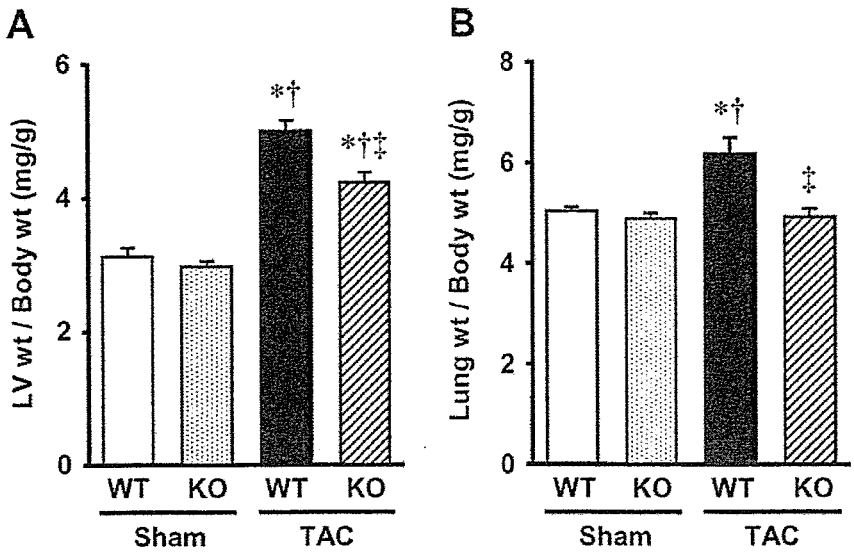

Figure 4. LV weight and lung weight from 4 groups of WT+Sham (n=6), KO+Sham (n=6), WT+TAC (n=9), and KO+TAC (n=10) mice. Values are mean±SEM. *P<0.01 vs WT+Sham; †P<0.01 vs KO+Sham; ‡P<0.01 vs WT+TAC.

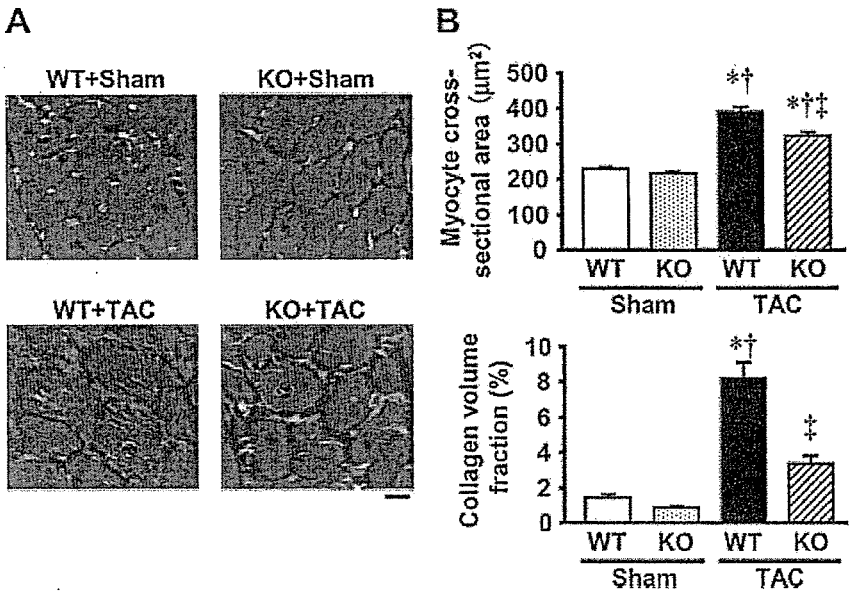

Figure 5. (A) Representative high-power photomicrographs of LV cross-sections stained with Masson's trichrome from 4 groups of WT+Sham, KO+Sham, WT+TAC, and KO+TAC mice. Scale bar, 10 μm. (B) Summary data of myocyte cross-sectional area (top) and collagen volume fraction (bottom) by the histomorphometric analysis of LV tissue sections from 4 groups of WT+Sham (n=4), KO+Sham (n=4), WT+TAC (n=5), and KO+TAC (n=5) mice. Values are mean±SEM. *P<0.01 vs WT+Sham; †P<0.01 vs KO+Sham; ‡P<0.01 vs WT+TAC.

diographic measurements for LV dimensions and FS were small, and the measurements made in the same animals on separate days were highly reproducible.[14] Therefore, our technique could be considered to allow for a noninvasive assessment of the LV structure and function. Second, the heart rate values in the present study (460 to 480 bpm) were lower than those (600 bpm) measured in conscious mice. Therefore, the LV size and function data might be greatly influenced by differences in anesthetic regimens and the experimental conditions, such as the heart rate. Third, MMP 9 was not increased in our model of PO hypertrophy. Although the present study could not provide the definite explanation for these results, they might be related to the small number of infiltrating inflammatory cells as neutrophils and macrophages, in which MMP 9 is mainly expressed, within the hypertrophied LV.

Perspectives

Diastolic dysfunction is an important factor contributing to the development of heart failure. One of the most common causes for diastolic heart failure is LV hypertrophy associated with hypertension. The present study demonstrated that MMP 2 inhibition reduced myocyte hypertrophy and interstitial fibrosis, which might contribute to a decrease in LV EDP and lung weight, an index of pulmonary congestion, without affecting LV systolic function. Therefore, although the present study did not directly evaluate the diastolic function itself, the reduction of LV EDP and lung congestion achieved with MMP 2 inhibition in this model is considered to be because of the attenuation of LV hypertrophy and the resultant improvement of diastolic function.

Conclusions

Chronic PO results in an initial cardiac hypertrophic response followed by progressive failure. Our findings provide the first direct evidence that MMP 2 is involved in mediating the adverse myocardial remodeling that occurs in response to a common form of hemodynamic overload. The beneficial effects of MMP 2 inhibition occurred in the absence of a decrease in systemic blood pressure. These findings suggest that the early institution of MMP 2 inhibition may have use in preventing the development of maladaptive myocardial remodeling in response to hypertension.

Acknowledgments

This study was supported in part by grants from the Ministry of Education, Science and Culture (No. 12670676, 14370230, and 17390223). A part of this study was conducted in Kyushu University Station for Collaborative Research I and II.

References

1. Redfield MM, Jacobsen SJ, Burnett JC Jr, Mahoney DW, Bailey KR, Rodeheffer RJ. Burden of systolic and diastolic ventricular dysfunction in the community: appreciating the scope of the heart failure epidemic. *JAMA*. 2003;289:194–202.
2. Spinale FG. Matrix metalloproteinases: regulation and dysregulation in the failing heart. *Circ Res*. 2002;90:520–530.
3. Peterson JT, Hallak H, Johnson L, Li H, O'Brien PM, Sliskovic DR, Bocan TM, Coker ML, Etoh T, Spinale FG. Matrix metalloproteinase inhibition attenuates left ventricular remodeling and dysfunction in a rat model of progressive heart failure. *Circulation*. 2001;103:2303–2309.
4. Sakata Y, Yamamoto K, Mano T, Nishikawa N, Yoshida J, Hori M, Miwa T, Masuyama T. Activation of matrix metalloproteinases precedes left ventricular remodeling in hypertensive heart failure rats: its inhibition as a primary effect of Angiotensin-converting enzyme inhibitor. *Circulation*. 2004;109:2143–2149.
5. Polyakova V, Hein S, Kostin S, Ziegelhoeffer T, Schaper J. Matrix metalloproteinases and their tissue inhibitors in pressure-overloaded human myocardium during heart failure progression. *J Am Coll Cardiol*. 2004;44:1609–1618.
6. Heymans S, Lupu F, Terclavers S, Vanwetswinkel B, Herbert JM, Baker A, Collen D, Carmeliet P, Moons L. Loss or inhibition of uPA or MMP-9 attenuates LV remodeling and dysfunction after acute pressure overload in mice. *Am J Pathol*. 2005;166:15–25.
7. Romanic AM, Harrison SM, Bao W, Burns-Kurtis CL, Pickering S, Gu J, Grau E, Mao J, Sathe GM, Ohlstein EH, Yue TL. Myocardial protection from ischemia/reperfusion injury by targeted deletion of matrix metalloproteinase-9. *Cardiovasc Res*. 2002;54:549–558.
8. Cheung PY, Sawicki G, Wozniak M, Wang W, Radomski MW, Schulz R. Matrix metalloproteinase-2 contributes to ischemia-reperfusion injury in the heart. *Circulation*. 2000;101:1833–1839.
9. Schubert A, Walther T, Falk V, Binner C, Loscher N, Kanev A, Bleiziffer S, Rauch T, Autschbach R, Mohr FW. Extracellular matrix gene expression correlates to left ventricular mass index after surgical

induction of left ventricular hypertrophy. *Basic Res Cardiol.* 2001;96: 381–387.
10. Hayashidani S, Tsutsui H, Ikeuchi M, Shiomi T, Matsusaka H, Kubota T, Imanaka-Yoshida K, Itoh T, Takeshita A. Targeted deletion of MMP-2 attenuates early LV rupture and late remodeling after experimental myocardial infarction. *Am J Physiol Heart Circ Physiol.* 2003;285: H1229–H1235.
11. Itoh T, Ikeda T, Gomi H, Nakao S, Suzuki T, Itohara S. Unaltered secretion of β-amyloid precursor protein in gelatinase A (matrix metalloproteinase 2)-deficient mice. *J Biol Chem.* 1997;272:22389–22392.
12. Rockman HA, Ross RS, Harris AN, Knowlton KU, Steinhelper ME, Field LJ, Ross J Jr, Chien KR. Segregation of atrial-specific and inducible expression of an atrial natriuretic factor transgene in an in vivo murine model of cardiac hypertrophy. *Proc Natl Acad Sci USA.* 1991;88: 8277–8281.
13. Matsusaka H, Ikeuchi M, Matsushima S, Ide T, Kubota T, Feldman AM, Takeshita A, Sunagawa K, Tsutsui H. Selective disruption of MMP-2 gene exacerbates myocardial inflammation and dysfunction in mice with cytokine-induced cardiomyopathy. *Am J Physiol Heart Circ Physiol.* 2005;289:H1858–H1864.
14. Shiomi T, Tsutsui H, Hayashidani S, Suematsu N, Ikeuchi M, Wen J, Ishibashi M, Kubota T, Egashira K, Takeshita A. Pioglitazone, a peroxisome proliferator-activated receptor-γ agonist, attenuates left ventricular remodeling and failure after experimental myocardial infarction. *Circulation.* 2002;106:3126–3132.
15. Liao Y, Ishikura F, Beppu S, Asakura M, Takashima S, Asanuma H, Sanada S, Kim J, Ogita H, Kuzuya T, Node K, Kitakaze M, Hori M. Echocardiographic assessment of LV hypertrophy and function in aortic-banded mice: necropsy validation. *Am J Physiol Heart Circ Physiol.* 2002;282:H1703–H1708.
16. Krege JH, Hodgin JB, Hagaman JR, Smithies O. A noninvasive computerized tail-cuff system for measuring blood pressure in mice. *Hypertension.* 1995;25:1111–1115.
17. Ishibashi Y, Tsutsui H, Yamamoto S, Takahashi M, Imanaka-Yoshida K, Yoshida T, Urabe Y, Sugimachi M, Takeshita A. Role of microtubules in myocyte contractile dysfunction during cardiac hypertrophy in the rat. *Am J Physiol.* 1996;271:H1978–H1987.
18. Namba T, Tsutsui H, Tagawa H, Takahashi M, Saito K, Kozai T, Usui M, Imanaka-Yoshida K, Imaizumi T, Takeshita A. Regulation of fibrillar collagen gene expression and protein accumulation in volume-overloaded cardiac hypertrophy. *Circulation.* 1997;95:2448–2454.
19. Chancey AL, Brower GL, Peterson JT, Janicki JS. Effects of matrix metalloproteinase inhibition on ventricular remodeling due to volume overload. *Circulation.* 2002;105:1983–1988.
20. Heymans S, Schroen B, Vermeersch P, Milting H, Gao F, Kassner A, Gillijns H, Herijgers P, Flameng W, Carmeliet P, Van de Werf F, Pinto YM, Janssens S. Increased cardiac expression of tissue inhibitor of metalloproteinase-1 and tissue inhibitor of metalloproteinase-2 is related to cardiac fibrosis and dysfunction in the chronic pressure-overloaded human heart. *Circulation.* 2005;112:1136–1144.
21. Nagatomo Y, Carabello BA, Coker ML, McDermott PJ, Nemoto S, Hamawaki M, Spinale FG. Differential effects of pressure or volume overload on myocardial MMP levels and inhibitory control. *Am J Physiol Heart Circ Physiol.* 2000;278:H151–H161.
22. Matsumura S, Iwanaga S, Mochizuki S, Okamoto H, Ogawa S, Okada Y. Targeted deletion or pharmacological inhibition of MMP-2 prevents cardiac rupture after myocardial infarction in mice. *J Clin Invest.* 2005; 115:599–609.
23. Wang GY, Bergman MR, Nguyen AP, Turcato S, Swigart PM, Rodrigo MC, Simpson PC, Karliner JS, Lovett DH, Baker AJ. Cardiac transgenic matrix metalloproteinase-2 expression directly induces impaired contractility. *Cardiovasc Res.* 2006;69:688–696.
24. Heymans S, Luttun A, Nuyens D, Theilmeier G, Creemers E, Moons L, Dyspersin GD, Cleutjens JP, Shipley M, Angellilo A, Levi M, Nube O, Baker A, Keshet E, Lupu F, Herbert JM, Smits JF, Shapiro SD, Baes M, Borgers M, Collen D, Daemen MJ, Carmeliet P. Inhibition of plasminogen activators or matrix metalloproteinases prevents cardiac rupture but impairs therapeutic angiogenesis and causes cardiac failure. *Nat Med.* 1999;5:1135–1142.
25. Ducharme A, Frantz S, Aikawa M, Rabkin E, Lindsey M, Rohde LE, Schoen FJ, Kelly RA, Werb Z, Libby P, Lee RT. Targeted deletion of matrix metalloproteinase-9 attenuates left ventricular enlargement and collagen accumulation after experimental myocardial infarction. *J Clin Invest.* 2000;106:55–62.
26. Nagase H, Woessner JF Jr. Matrix metalloproteinases. *J Biol Chem.* 1999:274:21491–21494.

Wireless Personal Communications (2006)
DOI 10.1007/s11277-006-9196-5

Performance of Super-Orthogonal Convolutional Coding for Ultra-Wideband Systems in Multipath and Multiuser Channels

TOMOKO MATSUMOTO and RYUJI KOHNO

Division of Physics, Electrical and Computer Engineering, Graduate School of Engineering, Yokohama National University, 79-5 Tokiwadai, Hodogaya-ku, Yokohama 240-8501, Japan
E-mail: tomoko@kohnolab.dnj.ynu.ac.jp

Abstract. This paper investigates the application of super-orthogonal convolutional codes (SOCC) to a direct-sequence based ultra-wideband (DS-UWB) system under a realistic environment including inter-symbol interference (ISI) and multiuser interference (MUI). The effect of MUI and ISI on the performance of SOCC is analyzed by using both maximum ratio combining (MRC) RAKE receiver and minimum mean-squared error (MMSE) RAKE receiver followed by matched filter receiver. The analysis shows that in the case of employing simple MRC-RAKE receiver, the performance of SOCC is affected by MUI and ISI because of the short length of the spreading sequence. In order to combat MUI and ISI, a code-hopping scheme is proposed in conjunction with SOCC. The results show that SOCC scheme outperforms the higher-rate conventional convolutional coded scheme for multipath and multiple access channels. Furthermore, the use of MMSE-RAKE receiver to suppress interference is analyzed and the subsequent increase of the system capacity is observed.

Keywords: ultra-wideband communications, super-orthogonal convolutional codes, code-spreading, RAKE receiver

Abbreviations: KAP – Kluwer Academic Publishers; compuscript – Electronically submitted article

1. Introduction

In recent years, ultra-wideband (UWB) technology has received considerable attention. UWB technology has some attractive features including high-data rate, multipath robustness, low cost, and low-power consumption. High-data rate wireless personal area network (HR-WPAN) is one of the applications of UWB technology. Another application is low-data rate WPAN (LR-WPAN), which provides relatively low-data rate transmission over medium range, combined with precise ranging and positioning capabilities.

Due to the large bandwidth, however, it is inevitable for UWB systems to coexist with other existing radio systems. In order to reduce the intra-system interference (ISI), UWB devices must meet stringent power spectral density requirements specified by regulations. This highlights the importance of power efficiency in the design of UWB systems. Therefore, applying strong forward error control codes (FEC) is necessary in order to minimize the impact of power limitation.

In wideband transmissions, very low-rate channel codes are used in conjunction with spreading (referred to as code-spreading), since the bandwidth expansion by error control coding can be utilized as a spreading gain. So far, this code-spreading has been considered

in spread-spectrum systems [1–4]. It is well known that the appropriate allocation of the total bandwidth expansion between coding and spreading can drastically increase the capacity of such wideband systems.

For this reason, the low-rate codes can possibly be applied to UWB system as well, with its spread-spectrum nature [5]. Furthermore, with its wider bandwidth as opposed to the spread-spectrum systems, UWB systems can employ very low-rate codes lower than those used in conventional spread-spectrum systems.

Among the low-rate channel codes, the super-orthogonal convolutional codes (SOCC) introduced in [1], are focused here. So far, the application of SOCC to a time-hopping-based UWB (TH-UWB) has been investigated under multiuser additive white Gaussian noise (AWGN) channel [6] and Rayleigh fading channel [7]. However, in [6,7], neither comparison between SOCC and other channel codes nor performance analysis under realistic UWB multipath fading channel have been achieved.

In this paper, the achievable performance of super-orthogonal (SO) convolutional coded UWB system in a realistic multipath fading channel proposed by IEEE 802.15.3 TG3a [8] is analyzed. The main reason for using SOCC is their near optimal performance and relatively low implementation complexity. In [9], Turbo code and low-density parity check (LDPC) code are applied to UWB system. In this paper, neither turbo nor LDPC code is considered because they increase decoding complexity and delay. It is obvious that our analysis is applicable when it is coupled with turbo coding. The problem in using SOCC for UWB transmission is that when one employs low-rate codes under the constraint where the total spreading factor is fixed, the length of the spreading sequence is shortened, yielding poor auto- and cross-correlation property among spreading codes. This leads to serious multi-user interference (MUI) and ISI. In order to combat such a poor correlation property of the spreading code, there are mainly two strategies, namely, random scrambling [10] and code-hopping. The code-hopping scheme with predetermined multiple sequence is employed in this paper, whereby it leads different interference from symbol to symbol and makes the interference probability density function from other users close to the Gaussian distribution. The performance of the SO coded schemes are compared with the conventional higher rate convolutional coded schemes for two different types of coherent RAKE receiver followed by matched filter, i.e., conventional maximum ratio combining (MRC) receiver and minimum mean squared error (MMSE) combining receiver. The latter type of receiver effectively combines multipath and suppress both MUI and ISI. Furthermore, it can work without knowledge of other user's information, including spreading sequence, received timing and channel impulse response, and so on. Instead, it utilizes the cyclostationarity of interference signals so that it is adopted to the code-hopping scheme. Our performance analysis shows that the SO coded scheme combined with the code-hopping scheme outperforms the conventional higher rate convolutional coded scheme under multipath and multiuser environment for both types of receivers. The organization of this paper is as follows. Section 2 gives the system model. In Section 3, the optimum combining weight of MRC and MMSE RAKE receiver and theoretical upper bound of the bit error rate (BER) are derived. In Section 4, the analysis is confirmed by computer simulations. Finally, in Section 5, conclusions are drawn.

2. System Description

In this section, after briefly describing the encoder and decoder structure of SOCC, the overall system model is described.

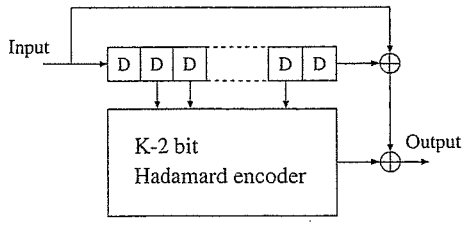

Figure 1. Encoder for SOCC of arbitrary constraint length K.

2.1. THE SUPER-ORTHOGONAL CONVOLUTIONAL CODES

Before describing the overall system model, it is useful to provide the encoder structure of SOCC and its important properties. The SOCC is a family of very low-rate orthogonal convolutional codes (VLORCC) proposed by Viterbi [1]. Figure 1 shows the SOCC encoder. The encoder has a shift register of length K and block orthogonal (Walsh-Hadamard) encoder. First, let us define the Walsh-Hadamard matrix as

$$\mathbf{H}_k = \begin{pmatrix} \mathbf{H}_{k-1} & \mathbf{H}_{k-1} \\ \mathbf{H}_{k-1} & \overline{\mathbf{H}}_{k-1} \end{pmatrix}, \quad \mathbf{H}_0 = 0, \tag{1}$$

where k is a nonzero integer, and $\overline{\mathbf{H}}_k$ is the complement of $\mathbf{H}_k$. In the K bit shift register, the inner $(K-2)$ bit memories are mapped into one Walsh sequence of length 2^{K-2}. Then, the remaining two outer bits are added to the selected Walsh sequence by modulo-2 addition. The resultant code rate is given by $R_c = 2^{-K+2}$.

The decoding is performed by using Viterbi algorithm (VA). In the trellis diagram of SOCC, there are two branches emanating from each state corresponding to two different bits. There are also two branches merging into each state. The mapping rule, adding the two outer memories to the selected Walsh sequence, guarantees that in the trellis diagram any two output sequences leaving and entering each state are complementary to each other. This effectively increases the minimum free distance of the codes compared to the previously proposed orthogonal and bi-orthogonal convolutional codes [1].

It should also be noted that as K increases the performance of SOCC is improved, approaching the Shannon capacity as $K \to \infty$. In addition to their near optimum performance, the SOCC has an additional advantage that the decoder structure is relatively simple because decoding is performed based on VA.

2.2. TRANSMIT SIGNAL MODEL

The overall system model considered is shown in Figure 2. At the transmitter, a binary information stream $\boldsymbol{d}_k \triangleq \left(d_0^k, d_1^k, \ldots, d_{N_b-1}^k\right)$ is encoded by a SOCC encoder of coding rate $R_c = 1/L_c$, where k and N_b denote the user number and the number of transmitted bits. The resultant stream of binary codewords are converted to antipodal signal stream $\boldsymbol{b}_k \triangleq \left(b_0^k, b_1^k, \ldots, b_{L_c N_b-1}^k\right)$, which is then spread by a user-specific spreading sequence. The

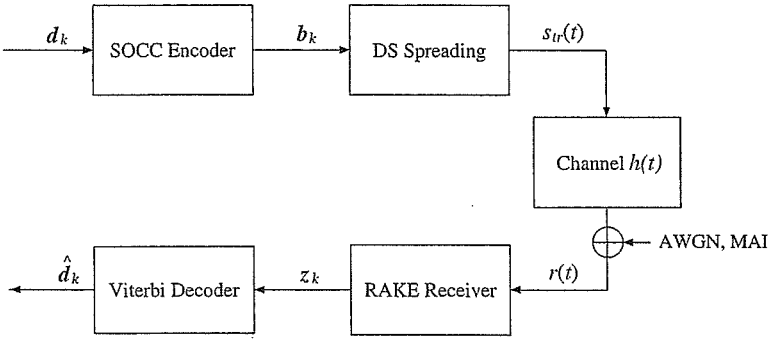

Figure 2. The overall system model of DS-UWB.

baseband transmit signal for the kth user is given by

$$s_{tr}^k(t) = \sum_{n=0}^{L_c N_b - 1} b_n^k p_n^k(t - nT_s), \tag{2}$$

where T_s denotes the symbol duration, and $p_n^k(t)$ is a signature waveform of duration T_s defined as

$$p_n^k(t) = \sqrt{\frac{E_s}{N_c}} \sum_{i=0}^{N_c - 1} c_i^k(n)\rho(t - nT_c), \tag{3}$$

where E_s denotes the symbol energy. The transmit pulse shape $\rho(t)$ is a Gaussian waveform of duration T_p, whose energy is normalized as $\int_0^{T_p} |\rho(t)|^2 dt = 1$. The pulse width is assumed to be less than the chip duration T_c, i.e., $T_p < T_c$. For simplicity, we assume $T_s = N_c T_c$. Let

$$\boldsymbol{c}^k(n) \triangleq \left[c_0^k(n), c_1^k(n), \ldots, c_{N_c-1}^k(n)\right]^T \tag{4}$$

denote a pseudo-random spreading sequence of length N_c, where $(\cdot)^T$ denotes transpose operation. The spreading sequence assumes the value of $\{\pm 1\}$ (DS spreading).

In this case, the total spreading factor can be represented as the product of two kinds of bandwidth expansion factor, i.e., $N = F_s F_c$, where $F_s = N_c$ and $F_c = 1/R_c$. The first term is the bandwidth expansion factor by spreading, and the second one is the bandwidth expansion factor by channel coding, and the two types of bandwidth expansion factors are freely interchangeable. Thus, the use of low-rate codes, under the constraint that the total spreading factor N is fixed, clearly, shortens the length of spreading sequence, which leads to poor correlation characteristics of the spreading sequences. In addition to this, it is well known that the correlation characteristics of the Walsh sequences, which are used as codewords of SOCC, are poor. This means that the SO coded UWB system suffers severely from MUI as well as ISI by considering that in typical UWB channel there exists hundreds of multipath having large delay-spread and many uncooperative UWB devices in other piconets.

In order to reduce the effect of ISI and MUI, the use of several spreading sequences per single user, which throughout of this paper is referred to as *code-hopping*, is proposed. In the code-hopping (CH) scheme, spreading sequences are switched between a predetermined set of sequences. This results in different interferences from symbol to symbol and makes the

interference probability density function (pdf) closely approximate the Gaussian distribution. We define the number of pre-determined sequence per single user as J. Let

$$\boldsymbol{a}^k = \left[\boldsymbol{a}^k(0), \boldsymbol{a}^k(1), \ldots, \boldsymbol{a}^k(J-1)\right] \tag{5}$$

be a set of sequences allocated for the kth user, where

$$\boldsymbol{a}^k(j) = \left[a_0^k(j), a_1^k(j), \ldots, a_{N_c-1}^k(j)\right]^T \in \{\pm 1\} \tag{6}$$

for $0 \leq j < J$. Then, the sequences are switched from symbol to symbol so that

$$\boldsymbol{c}^k(n) = \boldsymbol{a}^k(n \bmod J). \tag{7}$$

2.3. Received Signal Model

The signal $s_{\mathrm{tr}}(t)$ is transmitted through a channel having impulse response $h_k(t)$ written as [8]

$$h_k(t) = \sum_{l=1}^{L_{\max}} \alpha_l^k \delta(t - \tau_l^k), \tag{8}$$

where $L_{\max}$ is the number of multipath components, α_l^k and τ_l^k denote, respectively, the received amplitude and the delay of the lth path. The total energy of $h_k(t)$ is normalized, i.e., $\int_0^{T_{\max}} |h_k(t)|^2 dt = 1$, where $T_{\max}$ denotes the maximum delay spread.

Defining $\tilde{p}_n^k(t) = h_k(t) * p_n^k(t)$ as the received signature waveform, the received signal may be written as

$$\begin{aligned} s_{\mathrm{rec}}^k(t) &= \sum_{n=0}^{N_b-1} b_n^k \tilde{p}_n^k(t - nT_s) \\ &= \sum_{n=0}^{N_b-1} b_n^k \sum_{l=1}^{L_{\max}} \alpha_l^k \rho(t - nT_s - \tau_l). \end{aligned} \tag{9}$$

Assume that N_u transmitters are active, then the total received signal is represented as follows.

$$r(t) = \sum_{k=1}^{N_u} A_k s_{\mathrm{rec}}^k(t - \tau_k) + \nu(t), \tag{10}$$

in which A_k and τ_k are the channel attenuation and relative time offset between transmitted signal of the kth user and receiver of the desired user. Without loss of generality, assume the desired user as user 1. The AWGN with two-sided power spectral density $N_0/2$ is denoted by $\nu(t)$.

2.4. RAKE Receiver Structure

In this paper, a coherent RAKE receiver followed by matched filter (MF) is considered to exploit the multipath diversity and combat the fading inherent to realistic channels. Since in UWB channel there exists hundreds of multipath components, it is too expensive in terms of

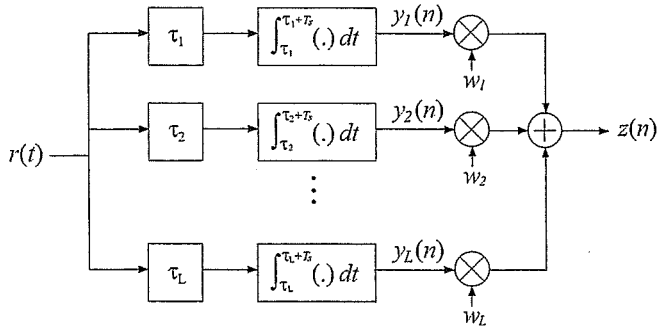

Figure 3. L-branch coherent RAKE receiver.

complexity to gather them all. Thus, we adopt a suboptimum method where only the largest L out of $L_{\max}$ paths are combined, called selective RAKE (S-RAKE) in the literature [11].

Let $\{\lambda_l\}_{l=1}^{L}$ and $\{\theta_l\}_{l=1}^{L}$ denote the estimation of the amplitude and delay, respectively, of the selected largest L paths. The subscript l is ordered by the delay time (i.e., $\theta_1 < \theta_2 < \cdots < \theta_L$). In order to make theoretical analysis tractable, the following assumptions are made. First, the synchronization between transmitter and receiver for desired user is perfectly established, i.e, $\tau_1 = 0$. Secondly, the receiver of the desired user can perfectly estimate the channel response $h_1(t)$ prior to data transmission by using some pilot symbols. Finally, the signature waveforms for all users have the same period, while the desired user's receiver does not know the timing offset τ_k or the channel response $h_k(t)$ for other interference users ($2 \leq k \leq N_u$). This assumption is valid considering that the typical UWB assumes peer-to-peer transmission.

Figure 3 shows the RAKE receiver structure considered in this paper. As shown in Figure 3, the receiver consists of a bank of L RAKE fingers, each correlating to a different delay of the received signal. Without loss of generality, we consider the nth symbol. Let $\boldsymbol{y}(n)$ denote the MF output given by

$$\boldsymbol{y}(n) = [y_1(n), y_2(n), \ldots, y_L(n)]^T , \tag{11}$$

whose elements denote the MF outputs corresponding to each path.

$$y_l(n) = \int_{\theta_l}^{\theta_l + T_s} r(t + nT_s) \cdot p_n^1(t - \theta_l) dt \tag{12}$$

for $0 \leq l < L$. The MF outputs are then combined to form a decision statistics. Let us define the combining weight for the coherent RAKE receiver as

$$\boldsymbol{w}(n) = [w_1(n), w_2(n), \ldots, w_L(n)]^T . \tag{13}$$

Note that the combining weight is a function of symbol index n when CH is employed since the received vector is changed from symbol to symbol. The derivation of the combining weight is shown in the next section. The decision statistic corresponding to the nth symbol is given by

$$z(n) = \boldsymbol{w}^T(n)\boldsymbol{y}(n). \tag{14}$$

By using the decision variable in (14), the decoding metric is calculated and decoding is performed by VA.

3. Performance Analysis

In this paper, two types of RAKE combining schemes, MRC combining and MMSE combining receivers, are considered. It is known that MRC is optimum under the AWGN channel, however it is not under other channels. On the contrary, MMSE combining receiver has the capability to effectively suppress the interferences such as ISI and MUI. In this section, the derivation of the combining weight for MRC and MMSE combining are, respectively, presented. Following, the upper bound of average BER is derived.

3.1. Derivation of the Combining Weight

Since the correlator output is composed of the sum of the signal components from all users, the MF outputs in (11) can be written as

$$\boldsymbol{y}(n) = \sum_{k=1}^{N_u} \boldsymbol{G}_k(n)\boldsymbol{b}_k(n) + \tilde{\boldsymbol{v}}(n), \tag{15}$$

where, the vector of length N_a $\boldsymbol{b}_k(n) = [b_0^k(n), \ldots, b_{N_a-1}^k(n)]^T \in \{\pm 1\}$ denotes the polarity of the kth user's signal, $\tilde{\boldsymbol{v}}(n) = \left[\tilde{v_1}(n), \tilde{v_2}(n), \ldots, \tilde{v_L}(n)\right]$ represents the noise term after despreading as

$$\tilde{v_l}(n) = \int_{\theta_l}^{\theta_l+T_s} v(t + nT_s)p_n^1(t - \theta_l)dt. \tag{16}$$

In (15), L-by-N_a matrix $\boldsymbol{G}_k(n)$ represents interference coefficients, where N_a is the maximum number of symbols in an observation time $T_w = \theta_L - \theta_1 + T_s$. In more details, N_a can be expressed as $N_a = N_l + N_r$, where $N_l = \lceil T_{max}/T_s \rceil$, $N_r = \lceil T_w/T_s \rceil$. The coefficient matrix $\boldsymbol{G}_k(n)$ is expressed as

$$\boldsymbol{G}_k(n) = \left[\boldsymbol{g}_1^k(n), \ldots, \boldsymbol{g}_{N_a}^k(n)\right]. \tag{17}$$

Each column vector

$$\boldsymbol{g}_i^k(n) = \left[g_{i,1}^k(n), \ldots, g_{i,L}^k(n)\right]^T \tag{18}$$

represents the interference coefficient from the ith symbol of the kth user. Note that $\boldsymbol{g}_{N_l}^1(n)$ represents the desired output. Each element of $\boldsymbol{g}_i^k(n)$ is expressed as

$$g_{i,l}^k(n) = \sum_{m=1}^{L_{max}} \alpha_m^k f_{1,k}\left(\tau_m^k + \tau_k + (i - N_l)T_s - \theta_l\right), \tag{19}$$

where $f_{1,k}(x)$ denotes the aperiodic cross-correlation function between $p_{1,n}(t)$ and $p_{k,i}(t)$

$$f_{1,k}(x) = \int_0^{T_s} p_{1,n}(t)p_{k,i}(t + x)dt. \tag{20}$$

Here, because of the independence assumption on the AWGN components as well as the interference from different users of different RAKE branches, the correlation matrix of MF outputs